

Controllable Mind Visual Diffusion Model

Bohan Zeng^{1,*}, Shanglin Li^{1,*}, Xuhui Liu¹, Sicheng Gao¹

Xiaolong Jiang³, Xu Tang³, Yao Hu³, Jianzhuang Liu², Baochang Zhang^{1,4†}

¹Beihang University ²Shenzhen Institute of Advanced Technology, Shenzhen, China

³Xiaohongshu Inc ⁴Zhongguancun Laboratory, Beijing, China

Abstract

Brain signal visualization has emerged as an active research area, serving as a critical interface between the human visual system and computer vision models. Although diffusion models have shown promise in analyzing functional magnetic resonance imaging (fMRI) data, including reconstructing high-quality images consistent with original visual stimuli, their accuracy in extracting semantic and silhouette information from brain signals remains limited. In this regard, we propose a novel approach, referred to as Controllable Mind Visual Diffusion Model (CMVDM). CMVDM extracts semantic and silhouette information from fMRI data using attribute alignment and assistant networks. Additionally, a residual block is incorporated to capture information beyond semantic and silhouette features. We then leverage a control model to fully exploit the extracted information for image synthesis, resulting in generated images that closely resemble the visual stimuli in terms of semantics and silhouette. Through extensive experimentation, we demonstrate that CMVDM outperforms existing state-of-the-art methods both qualitatively and quantitatively.

1 Introduction

Understanding the cognitive processes that occur in the human brain when observing visual stimuli (e.g., natural images) has long been a primary focus for neuroscientists. Both objective visual stimuli and subjective cognitive activities can elicit the transmission of intricate neural signals in the visual cortex of the brain, thus laying the foundation for higher-order cognitive and decision-making processes. With the advancement of techniques such as functional magnetic resonance imaging (fMRI), it has become possible to capture real-time brain activity signals with greater accuracy and finer granularity, thereby accelerating the progress of neuroscientific research. Deciphering and reconstructing from these intricate signals remain a great challenge to both cognitive neuroscience and downstream applications like Brain-Computer Interfaces (BCI) [1, 2].

Early attempts [3, 4, 5, 6] of analyzing brain activity on visual tasks mainly focus on matching human subjects' brain activity with observed natural images, or reconstructing visual patterns of simple geometric shapes [7, 8, 9]. These explorations demonstrate the feasibility to derive semantic information for perceived images from brain signals, yet they have poor generalization to unseen semantic categories or complicated reconstruction tasks. Recent studies [10, 11, 12, 13, 14] have made significant progress in reconstructing visual stimuli from brain signals. [10, 11] can generate images that are similar in shape to the original visual stimuli, but the images suffer from severe distortion and blur issues. [12, 13, 14] have employed commonly used generative models, such as Generative Adversarial Networks (GAN) or diffusion models, to generate high-quality RGB images that maintain semantic consistency with the original visual stimuli conditioned on corresponding fMRI signals. However, such methods struggle with positional inconsistency, as shown in Fig. 1. In

*These authors contributed equally.

†Corresponding Author: bczhang@buaa.edu.cn.

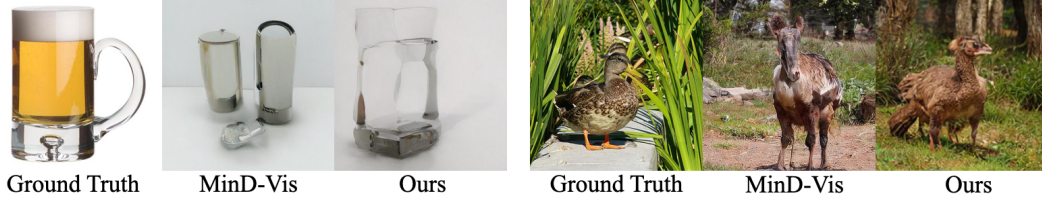


Figure 1: Illustration of synthesis results. A recent method MinD-Vis [13] can generate photo-realistic results, but they cannot well match the visual stimuli in terms of semantics and silhouette. Our method can generate better results more consistent with the visual stimuli.

general, existing methods have not effectively utilized the semantic and spatial features inherent in fMRI signals.

In this paper, we present a Controllable Mind Visual Diffusion Model (CMVDM) that enables the mind diffusion model with a control network to leverage the extracted faithful semantic and silhouette information for high-fidelity human vision reconstruction. Specifically, we first finetune a pretrained latent diffusion model (LDM) with a semantic alignment loss and pretrain a silhouette extractor to estimate accurate semantic and silhouette information of the fMRI data. Taking inspiration from ControlNet [15], we then introduce a control network, which takes the silhouette information as a condition, into the pretrained LDM to guide the diffusion process to generate desired images that match the original visual stimuli in terms of both semantic and silhouette information. Fig. 1 shows two examples where CMVDM outperforms the state-of-the-art approach, MinD-Vis [13].

In summary, the main contributions of this paper are as follows:

- We propose a novel Controllable Mind Visual Diffusion Model (CMVDM) that leverages both semantic and spatial visual patterns in brain activity to reconstruct photo-realistic images. A control network is utilized to enable effective manipulation over the positions of generated objects or scenes in the reconstructed images, providing a much better structural similarity to the original visual stimuli.
- We design two extractors to extract semantic and silhouette attributes to provide accurate information for generating images that closely resemble the visual stimuli. Besides, we build a residual module to provide information beyond semantics and silhouette.
- We conduct comprehensive experiments on two datasets to evaluate the performance of our CMVDM. It achieves state-of-the-art qualitative and quantitative results compared to existing methods, demonstrating the efficacy of CMVDM for generating high-quality and controllable images from fMRI signals.

2 Related Work

Diffusion Probabilistic Models. Diffusion models (DMs) were initially introduced by [16] as a novel generative model that gradually denoises images corrupted by Gaussian noise to produce samples. Recent advances in DMs have demonstrated their superior performance in image synthesis, with notable models including [17, 18, 19, 20, 21, 22]. DDGAN [23] is a model that reduces the number of sampling steps by directly predicting the ground truth in each timestep. DMs have also achieved state-of-the-art performance in other synthesis tasks, such as text-to-image generation with GLIDE [24], speech synthesis with [25, 26], and super-resolution with [27, 28, 29]. In addition, DMs have been applied to text-to-3D synthesis in [30, 31], and other 3D object syntheses in [32, 33, 34]. Furthermore, DMs have found applications in video synthesis [35, 36], semantic segmentation [37], text-to-motion generation [38], face animation [39], and object detection [40]. [41, 42] are models that generate diverse results by learning the internal patch distribution from a single image. ControlNet [15] employs a control network on a pretrained text-conditioned LDM for controllable image synthesis. Overall, DMs have shown promising results and have been widely adopted in various synthesis tasks.

Neural Decoding of Visual Stimuli. Neural decoding of visual stimuli has been a topic of growing interest in recent years. Numerous studies have explored the possibility of using machine learning

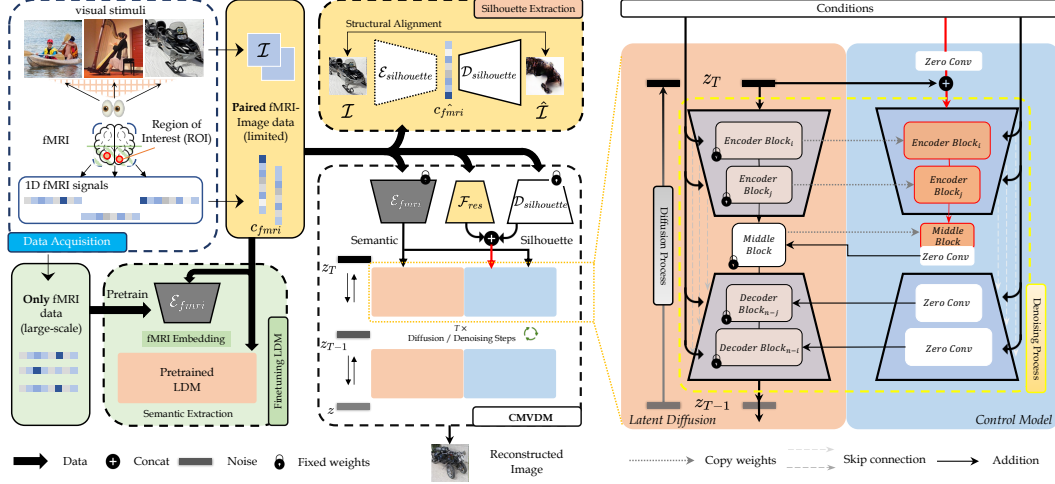


Figure 2: Overview of our proposed method. Initially, we train \mathcal{E}_{fMRI} and $\mathcal{D}_{silhouette}$ in the “Finetuning LDM” and “Silhouette Extraction” parts, respectively. Subsequently, we utilize \mathcal{E}_{fMRI} , $\mathcal{D}_{silhouette}$, and \mathcal{F}_{res} to extract semantic, silhouette, and supplement information from fMRI signals as conditions. Finally, we integrate the control network with the LDM to generate high-fidelity and controllable results tailored to the aforementioned conditions.

algorithms to decode visual information from patterns of neural activity in the human brain. For instance, [43] demonstrates that it is possible to reconstruct natural images from fMRI data using a linear decoder. Similarly, [44] shows that the orientation of gratings from patterns of activity in the early visual cortex can be decoded using a support vector machine. More recent studies have built on these findings by exploring more complex visual stimuli, such as natural scenes [45] and faces [46], and by developing more sophisticated machine learning algorithms, such as deep neural networks [47]. To enable decoding of novel scenarios, some works use an identification-based approach [5, 6, 44], where they model the relationship between brain activity and visual semantic knowledge such as image features extracted by a CNN [5, 6]. These studies provide valuable insights into the interpretation of human brain signals in the visual cortex, which can help the development of more effective and reliable decoding algorithms for a wide range of neuroimaging applications, such as Brain-Computer Interfaces [1]. However, these methods require a large amount of paired stimuli-responses data, which is hard to obtain. Therefore, decoding novel image categories accurately remains a challenge.

fMRI-to-Image Reconstruction With the remarkable advancements in generative models, recent studies have focused on the reconstruction of images from human brain activity. These studies employ various approaches, such as building an encoder-decoder structure to align image features with corresponding fMRI data, as demonstrated by [10] and [11]. To further enhance the quality of image reconstruction, researchers have turned to more sophisticated techniques, including generative adversarial networks (GAN) [12] and diffusion models [14, 13]. These methods have shown significant promise in achieving more plausible image reconstruction. Nonetheless, the approaches described above have limitations in terms of image reconstruction quality and localization accuracy, resulting in unreliable reconstruction outcomes and inadequate utilization of the deep semantic and shallow positional information inherent in fMRI signals.

3 Method

In this section, we describe the CMVDM model, which combines attribute extractors and a control model to produce precise and controllable outcomes from fMRI signals. Fig. 2 illustrates the architecture of CMVDM.

3.1 Problem Statement and Overview of CMVDM

Let the paired {fMRI, image} dataset $\Omega = \{(c_{fmri,i}, \mathcal{I}_i)\}_{i=1}^n$, where $c_{fmri,i} \in \mathbb{R}^{1 \times N}$ and $\mathcal{I}_i \in \mathbb{R}^{H \times W \times 3}$. The fMRI data is extracted as a 1D signal from the region of interest (ROI) on the visual cortex averaged across the time during which the visual stimuli are presented. N denotes the number of voxels of the extracted signal. We adopt the pretrained image encoder of the LDM [21] to encode the observed image \mathcal{I} into the latent code z . Our CMVDM aims to learn an estimation of the data distribution $p(z|c_{fmri})$ through a Markov chain with T timesteps. Following [17, 18, 21], we define the fixed forward Markov diffusion process q as:

$$q(z_{1:T} | z_0) = \prod_{t=1}^T q(z_t | z_{t-1}), \quad q(z_t | z_{t-1}) = \mathcal{N}\left(z_t | \sqrt{1 - \beta_t} z_{t-1}, \beta_t \mathbf{I}\right), \quad (1)$$

where z_0 denotes the latent code of an image. This Markov diffusion process propagates by adding Gaussian noise, with variances $\beta_t \in (0, 1)$ in T iterations. Given z_0 , the distribution of z_t can be represented by:

$$q(z_t | z_0) = \mathcal{N}(z_t | \sqrt{\gamma_t} z_0, (1 - \gamma_t) \mathbf{I}), \quad (2)$$

where $\gamma_t = \prod_{i=1}^t (1 - \beta_i)$. In the inference process, CMVDM learns the conditional distributions $p_\theta(z_{t-1} | z_t, c_{fmri})$ and conducts a reverse Markov process from Gaussian noise $z_T \sim \mathcal{N}(\mathbf{0}, \mathbf{I})$ to a target latent code z_0 as:

$$\begin{aligned} p_\theta(z_{0:T} | c_{fmri}) &= p(z_T) \prod_{t=1}^T p_\theta(z_{t-1} | z_t, c_{fmri}), \\ p(z_T) &= \mathcal{N}(z_T | \mathbf{0}, \mathbf{I}), \\ p_\theta(z_{t-1} | z_t, c_{fmri}) &= \mathcal{N}(z_{t-1} | \mu_\theta(c_{fmri}, z_t, t), \sigma_t^2 \mathbf{I}), \end{aligned} \quad (3)$$

where $\sigma_t = \frac{1 - \gamma_{t-1}}{1 - \gamma_t} \beta_t$. The pretrained image decoder of the LDM [21] turns the final latent code to an image.

Furthermore, we extract the attributes and control the generated results. Firstly, we extract the semantic and silhouette information by utilizing the fMRI encoder \mathcal{E}_{fmri} and the silhouette estimating network $\mathcal{D}_{silhouette}$, respectively. This step enables us to accurately analyze the fMRI information c_{fmri} . Subsequently, we utilize the control model $\mathcal{F}_{control}$ to generate high-quality images that match the visual stimuli in terms of both semantic and silhouette information. $\mathcal{F}_{control}$ is able to leverage the extracted information to produce better results. Besides, the residual module \mathcal{F}_{res} is designed to provide information beyond semantics and silhouette.

3.2 Finetuning of the Pretrained LDM

Before extracting the silhouette information and controlling the generated results, we need to finetune the pretrained LDM [21] to enable it to generate consistent images and extract the semantic information based on the input fMRI signals. Following MinD-Vis [13], we employ the fMRI encoder \mathcal{E}_{fmri} pretrained on the HCP dataset [48] to encode the brain activity signals to the semantic embeddings. Besides, we use the pretrained LDM to generate output images. By optimizing the fMRI encoder \mathcal{E}_{fmri} and the cross-attention layers in the LDM, while freezing the other blocks during the finetuning process, we can obtain reliable consistent generated results. The finetuning loss is defined as follows:

$$\mathcal{L}_1 = \mathbb{E}_{z_0, t, c_{fmri}, \epsilon \sim \mathcal{N}(\mathbf{0}, \mathbf{I})} [\|\epsilon - \epsilon_\theta(z_t, t, \mathcal{E}_{fmri}(c_{fmri}))\|_2^2], \quad (4)$$

where ϵ_θ is the denoising network of the LDM. In this way, the LDM can not only ensure the consistency of the generated results but also extract more reliable semantic embeddings. Let $c_{context} = \mathcal{E}_{fmri}(c_{fmri})$ be the semantic information extracted from the fMRI signals. Due to the lack of direct semantic information supervision, sometimes \mathcal{E}_{fmri} may misunderstand the semantic information of the fMRI signals. So we design a semantic alignment loss \mathcal{L}_{align} to further enhance the semantic information $c_{context}$:

$$\mathcal{L}_{align} = e^{-\cosine(f_{image, \text{MLP}(c_{context}))}, \quad (5)$$

where $\text{cosine}(\cdot, \cdot)$ denotes the cosine similarity, f_{image} is the image feature extracted by the CLIP image encoder [49], and MLP represents a trainable multi-layer perceptron. After this training stage, the LDM can make the generated images consistent with the fMRI signals. Nonetheless, due to the absence of explicit positional condition guidance, it is still a challenge for the LDM to generate silhouette-matched results. In the next two sections, we will describe how to extract silhouette information from the fMRI signals and control the final results.

3.3 Silhouette Extraction

In this section, we aim to extract silhouette information from fMRI signals. [11] uses a combination of self-supervised and supervised learning to reconstruct images similar to visual stimuli. The self-supervised process can be simply represented as: $\hat{\phi}_i = \mathcal{D}_{silhouette}(\mathcal{E}_{silhouette}(\phi_i))$, where $\phi_i \in \Phi$ denotes images from ImageNet [50]. Despite the low fidelity of the image generation quality, their generated results demonstrate a notable ability to accurately replicate the silhouette of the visual stimuli (see Fig. 3). Based on this, we devise a silhouette estimation network that is capable of providing rough positional guidance for CMVDM.

Our silhouette estimation network consists of two symmetrical components: an encoder $\mathcal{E}_{silhouette}$ and a decoder $\mathcal{D}_{silhouette}$. The encoder $\mathcal{E}_{silhouette}$ projects the input images to the fMRI signal space, while the decoder $\mathcal{D}_{silhouette}$ performs the inverse transformation.

Let $c_{fMRI,i}$ be the ground truth (GT) fMRI signal, $c_{fMRI,i} = \mathcal{E}_{silhouette}(\mathcal{I}_i)$ be the estimated fMRI signal, and $\theta_i \in \Theta$ denotes the parameters of $\mathcal{E}_{silhouette}$. We define the encoder training loss \mathcal{L}_e by a combination of the Mean Square Error (MSE) loss and cosine similarity:

$$\mathcal{L}_e = \frac{1}{|\Omega|} \sum_{i=1}^{|\Omega|} \left[\alpha_1 \cdot \|c_{fMRI,i} - c_{fMRI,i}\|^2 + \alpha_2 \cdot (1 - \text{cosine}(c_{fMRI,i}, c_{fMRI,i})) \right] + \alpha_3 \cdot \sum_{i=1}^{|\Theta|} |\theta_i|, \quad (6)$$

where $\alpha_{i \in \{1,2,3\}}$ are the hyperparameters set empirically to $\alpha_1 = 1$, $\alpha_2 = 0.3$ and $\alpha_3 = 0.001$. The inclusion of the L1 regularization in \mathcal{L}_e helps to prevent overfitting by promoting sparsity in the model’s parameters, ultimately leading to a simpler and more generalizable model.

After completing the training of $\mathcal{E}_{silhouette}$, we fix its parameters and train the reverse process for the decoder $\mathcal{D}_{silhouette}$. Due to the limited availability of paired {fMRI, image} data, mapping fMRI signals to images is challenging. Inspired by [11], we utilize semi-supervised training to extract intricate silhouette information. We employ the Structural Similarity (SSIM) loss besides the Mean Absolute Error (MAE) loss to penalize the spatial distances between the reconstructed images and the GT images. Let $\psi_i \in \Psi$ be the parameters of $\mathcal{D}_{silhouette}$. The two losses are:

$$\mathcal{L}_{MAE} = \underbrace{\beta_1 \cdot \frac{1}{|\Omega|} \sum_{i=1}^{|\Omega|} |\hat{\mathcal{I}}_i - \mathcal{I}_i|}_{supervised} + \underbrace{\beta_2 \cdot \frac{1}{|\Phi|} \sum_{i=1}^{|\Phi|} |\hat{\phi}_i - \phi_i|}_{self-supervised} + \beta_3 \cdot \sum_{i=1}^{|\Psi|} |\psi_i|, \quad (7)$$

$$\mathcal{L}_{SSIM} = \beta_4 \cdot \frac{(2\mu_{\mathcal{I}}\mu_{\hat{\mathcal{I}}} + C_1)(2\sigma_{\mathcal{I}\hat{\mathcal{I}}} + C_2)}{(\mu_{\mathcal{I}}^2 + \mu_{\hat{\mathcal{I}}}^2 + C_1)(\sigma_{\mathcal{I}}^2 + \sigma_{\hat{\mathcal{I}}}^2 + C_2)}, \quad (8)$$

where $\mu_{\hat{\mathcal{I}}}$, $\mu_{\mathcal{I}}$, $\sigma_{\hat{\mathcal{I}}}$, and $\sigma_{\mathcal{I}}$ represent the mean and std values of the reconstructed images $\hat{\mathcal{I}}$ and GT images \mathcal{I} , C_1 and C_2 are constants to stabilize the calculation, the last term in \mathcal{L}_{MAE} is for regularization, and $\beta_{i \in \{1,2,3,4\}}$ are set to 1, 1, 0.001 and 1 respectively.

The decoder loss \mathcal{L}_d is defined as the combination of the two losses:

$$\mathcal{L}_d = \mathcal{L}_{MAE} + \mathcal{L}_{SSIM}. \quad (9)$$

After training, $\mathcal{D}_{silhouette}$ is able to generate images $\hat{\mathcal{I}}$ from c_{fMRI} that provide positional guidance for CMVDM. To avoid confusion, we’ll refer to $\hat{\mathcal{I}}$ as $c_{silhouette}$ in the following section.

3.4 Control Model Training

After obtaining the enhanced semantic information $c_{context} = \mathcal{E}_{fmri}(c_{fmri})$ and the reliable silhouette information $c_{silhouette} = \mathcal{D}_{silhouette}(c_{fmri})$ from c_{fmri} , we use them to control the generated results as shown in Fig. 2. Inspired by ControlNet [15], we design a control model to control the overall composition of the generated images. Specifically, we freeze all the parameters in the denoising network ϵ_θ and clone the U-Net encoder of ϵ_θ into the trainable $\mathcal{F}_{control}(\cdot; \Theta_c)$ with a set of parameters Θ_c (the red blocks of Control Model in Fig. 2). The inputs of $\mathcal{F}_{control}$ include z_t , $c_{context}$, and the silhouette feature $c_{silhouette}$. The combined condition code $x'_{c,t}$ can be formulated as:

$$x'_{c,t} = \mathcal{Z}(\mathcal{F}_{control}(z_t + \mathcal{Z}(c_{silhouette}), c_{context}; \Theta_c)). \quad (10)$$

where $\mathcal{Z}(\cdot)$ denotes the zero convolution operation [15]. Besides, to make up for the fMRI information lost in the attribute extraction, we employ a trainable residual block \mathcal{F}_{res} to add information beyond semantics and silhouette. The final combined condition code $x_{c,t}$ is represented as:

$$x_{c,t} = \mathcal{Z}(\mathcal{F}_{control}(z_t + \mathcal{Z}(c_{silhouette} + \mathcal{Z}(\mathcal{F}_{res}(c_{fmri}))), c_{context}; \Theta_c)). \quad (11)$$

Then the output features $x_{c,t}$ of the control model are added to the U-Net decoder features of the frozen ϵ_θ , as shown in Fig. 2.

Finally, we use the following loss $\mathcal{L}_{control}$ to supervise the training of the control model and \mathcal{F}_{res} in our CMVDM:

$$\mathcal{L}_{control} = \mathbb{E}_{z_0, t, c_{fmri}, \epsilon \sim \mathcal{N}(0,1)} [\|\epsilon - \epsilon_\theta(z_t, t, c_{context}, x_{c,t})\|_2^2]. \quad (12)$$

Note that with their losses, the control model training, the pretrained LDM finetuning (Section 3.2), and the $\mathcal{D}_{silhouette}$ training (Section 3.3) are independent.

4 Experiments

4.1 Datasets and Implementation

Datasets. In this study, we employ two public datasets with paired fMRI signals and images: Generic Object Decoding (GOD) dataset [5], and Brain, Object, Landscape Dataset (BOLD5000) [51]. The GOD dataset is a well-known and extensively researched collection of fMRI-based brain signal decoding data. It comprises 1250 distinct images belonging to 200 different categories, with 50 images designated for testing. The BOLD5000 dataset is a rich resource for studying the neural representation of visual stimuli, as it contains diverse images from natural and artificial domains. The images are drawn from three existing datasets: SUN [52], COCO [53], and ImageNet [50], which contain images of various categories of objects and animals. BOLD5000 was acquired from four subjects who underwent fMRI scanning while viewing 5,254 images in 15 sessions. The fMRI data were preprocessed and aligned to a common anatomical space, resulting in 4803 fMRI-image pairs for training and 113 for testing. The dataset provides a unique opportunity to investigate how the human brain encodes visual information across different levels of abstraction and complexity. Additionally, we use the large-scale fMRI data from Human Connectome Project (HCP) [48] in an unsupervised manner to pretrain the fMRI encoder \mathcal{E}_{fmri} in our method, which aims to fully extract the features of fMRI signals.

Training Details. We adopt 1 A100-SXM4-40GB GPU for the training of \mathcal{E}_{fmri} and the control model, and 1 V100-SXM2-32GB GPU for $\mathcal{D}_{silhouette}$ training. Both \mathcal{E}_{fmri} and the control model are trained by the AdamW [54] with $\beta = (0.9, 0.999)$ and $eps = 1e - 8$ for 500 epochs. $\mathcal{D}_{silhouette}$ is optimized using Adam [55] with a learning rate of $5e - 3$ and $\beta = (0.5, 0.99)$ for 150 epochs.

4.2 Evaluation Metrics

N-way Classification Accuracy (Acc). Following [11, 13], we employ the n -way top-1 classification task to evaluate the semantic correctness of the generated results, where multiple trials for top-1 classification accuracies are calculated in $n - 1$ randomly selected classes with the correct class. Specifically, we follow MinD-Vis [13] and use a pretrained ImageNet-1K classifier [56] to estimate

Table 1: Quantitative comparison with four state-of-the-art (SOTA) methods. Bold results denote the best results and underline results denote the second-best results.

Method	GOD			BOLD5000		
	Acc (%)	PCC	SSIM	Acc(%)	PCC	SSIM
Beliy (2019)	4.288	0.48285	0.51795	/	/	/
Gaziv (2022)	9.128	<u>0.68326</u>	0.64857	/	/	/
IC-GAN (2022)	<u>29.386</u>	0.44857	0.54489	/	/	/
MinD-Vis (2023)	26.644	0.53159	0.52669	<u>25.918</u>	<u>0.54486</u>	<u>0.52379</u>
CMVDM (Ours)	30.112	0.76751	<u>0.63167</u>	27.791	0.55691	0.53459

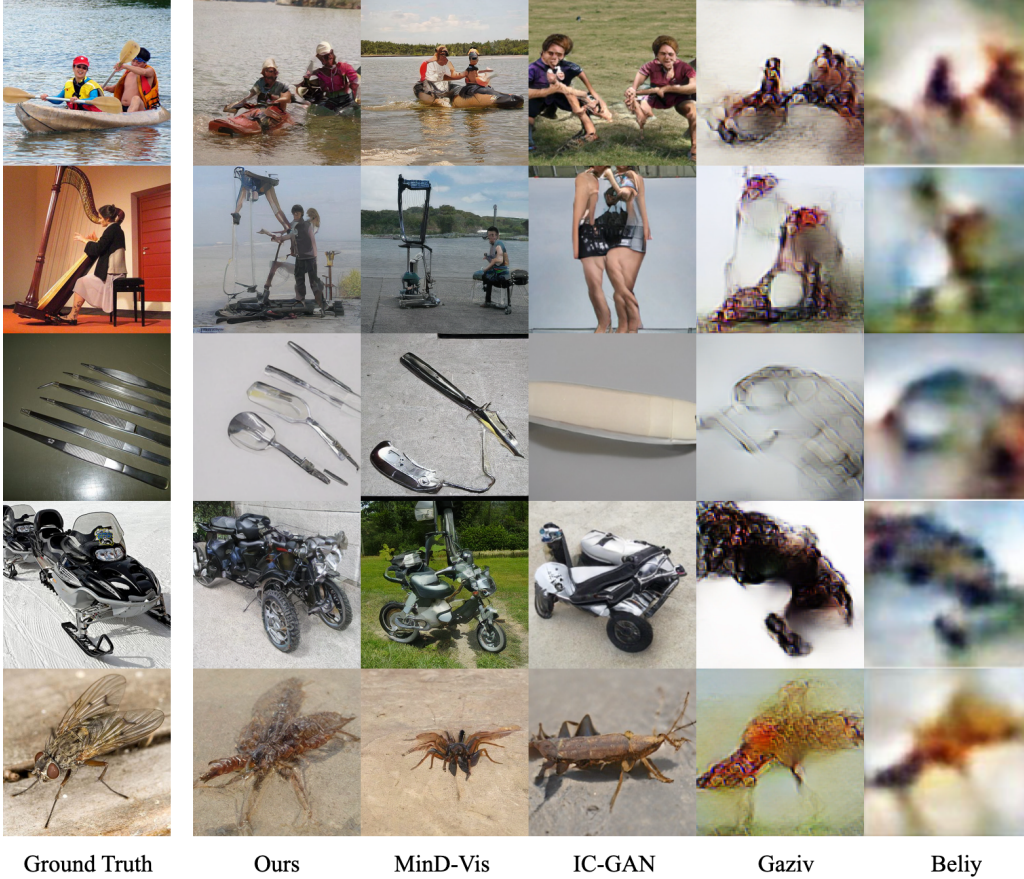


Figure 3: Comparison with four SOTA methods on the GOD dataset.

the accuracy. Firstly, we input the generated results and the ground-truth images into the classifier, and then check whether the top-1 classification matches the correct class. More details about this metric can be found in [13].

Pearson Correlation Coefficient (PCC). The Pearson correlation coefficient (PCC) measures the degree of linear association between two variables. PCC calculates the strength and direction of the relationship between two variables, with +1 indicating a perfect positive linear relationship and -1 indicating a perfect negative linear relationship. The larger the PCC value, the stronger the relationship between visual stimuli and generated images.

Structure Similarity Index Measure (SSIM). We adopt SSIM to evaluate the reconstruction faithfulness of the generated results. As analyzed in [57], the structural similarity of two images is measured by three different factors, brightness, contrast, and structure, where the mean is used as the



Figure 4: Comparison with MinD-Vis on the BOLD5000 dataset.

Table 2: Ablation study of CMVDM’s components.

Method	Acc (%)	PCC	SSIM
MinD-Vis	26.644	0.53159	0.54489
MinD-Vis+ \mathcal{L}_{align}	27.362	0.56686	0.52628
MinD-Vis+Control Model	28.438	0.75730	0.63404
CMVDM	30.112	0.76751	0.63167

estimate of brightness, the standard deviation as the estimate of contrast, and the covariance as the measurement of structural similarity.

4.3 Comparison with State-of-the-Art Methods

Methods. We compare our CMVDM with four state-of-the-art (SOTA) methods: MinD-Vis [13], IC-GANs [12], Gaziv [11], and Beliy [10]. We use their official pretrained models for all the comparisons, which are trained on the GOD dataset. For the BOLD5000 dataset, we only compare with the official pretrained MinD-Vis model, because other works [10, 11, 12] did not conduct experiments and release their models on BOLD5000.

Results on the GOD Dataset. We conduct a quantitative comparison between our CMVDM and the four SOTA models using the testing dataset of GOD. Table 1 summarizes the results, revealing that our CMVDM overall outperforms the other methods significantly. Compared to MinD-Vis and IC-GAN, both of which yield good results, our CMVDM outperforms them significantly in terms of SSIM. This indicates that the images generated by CMVDM exhibit a higher degree of resemblance to the visual stimuli in terms of object silhouette and image structure. Additionally, Fig. 3 displays the results of the methods. It is evident that our CMVDM generates visually impressive images whose semantic and silhouette information is closest to the visual stimuli. Although Gaziv achieves comparable results in terms of SSIM, its accuracy scores reported in Table 1 and its visual results presented in Fig. 3 demonstrate that Gaziv is not capable of generating high-fidelity images.

Results on the BOLD5000 Dataset. We conduct a comparative analysis between our CMVDM and the most recent method MinD-Vis using the testing dataset of BOLD5000. As depicted in Table 1, it is evident that CMVDM consistently outperforms MinD-Vis across all evaluation metrics. Additionally, Fig. 4 provides visualizations of some results from both methods, clearly demonstrating that CMVDM generates more realistic outcomes with silhouettes and positions that are closer to the viewed images. Notably, the BOLD5000 dataset, being more complex than the GOD dataset, further validates the effectiveness of our proposed method.



Figure 5: Consistency analysis of the generated results.

Table 3: Quantitative analysis of the residual block in CMVDM.

Dataset	Method	Acc(%)	PCC	SSIM
BOLD5000	w/o \mathcal{F}_{res}	25.393	0.54184	0.52951
	w \mathcal{F}_{res}	27.791	0.55691	0.53459
GOD	w/o \mathcal{F}_{res}	29.436	0.75837	0.63894
	w \mathcal{F}_{res}	30.112	0.76751	0.63167

4.4 Ablation Study

We further conduct experiments on the GOD dataset to analyze the effectiveness of each module of our CMVDM. Specifically, we employ MinD-Vis [13] as the baseline and design two comparison models: (1) adding the semantic align loss \mathcal{L}_{align} to MinD-Vis, (2) adding the control model to MinD-Vis. The results, presented in Table 2, demonstrate the efficacy of both \mathcal{L}_{align} and the control model within our CMVDM. MinD-Vis with \mathcal{L}_{align} yields improved results in terms of ACC and PCC, which illustrate that \mathcal{L}_{align} can improve the capability of CMVDM to obtain semantic information. Furthermore, MinD-Vis+Control Model outperforms MinD-Vis+ \mathcal{L}_{align} in each metric, particularly in SSIM, indicating that the silhouette contains valuable semantic information that is used in the control model.

4.5 Consistency Analysis

To further verify the generative stability of CMVDM, we conduct an analysis to compare the consistency of two diffusion model-based methods. As shown in Figure 5, we sample four images reconstructed by CMVDM and MinD-Vis from the same fMRI signal. The images generated by CMVDM demonstrate a high degree of consistency to GT image both semantically and structurally. However, the results generated by MinD-Vis are capable of reproducing GT image semantically but are not consistent in structure.

4.6 Further Analysis

The impact of using the residual module \mathcal{F}_{res} in our CMVDM is significant on the BOLD5000 dataset, as demonstrated in Table 3. However, the effect of \mathcal{F}_{res} on the GOD dataset is not as pronounced. We believe that there are two reasons for this discrepancy. Firstly, the voxels of a single fMRI signal provided by the BOLD5000 dataset are much less than that provided by the GOD dataset, making it more challenging to extract valid semantic and silhouette information from BOLD5000. Therefore, \mathcal{F}_{res} is necessary to compensate for the information gap. Secondly, compared to GOD, BOLD5000 has more diverse images, including scenes that are not present in GOD. The semantic judgment and position alignment of the images in BOLD5000 are more complex than those in GOD. Therefore, we utilize \mathcal{F}_{res} to provide more information and improve the reconstruction performance.

5 Conclusion

In this paper, we propose a Controllable Mind Visual Diffusion Model (CMVDM) for decoding fMRI signals. Firstly, we simultaneously train a semantic encoder and perform finetuning on a pretrained latent diffusion model to generate semantically consistent images from fMRI signals. Secondly, we incorporate a silhouette extractor to derive reliable position information from the fMRI signals. Furthermore, we design a control model to ensure CMVDM generates semantically-consistent and spatially-aligned images with the original visual stimuli. Extensive experiments demonstrate that our approach achieves state-of-the-art performance in generating high-quality images from fMRI signals.

6 Social Impact

This work does not have a direct negative social impact. However, we should pay attention to the ethical and privacy issues in the process of collecting or using our model to visualize fMRI signals and prevent them from being abused for malicious purposes.

References

- [1] L. F. Nicolas-Alonso and J. Gomez-Gil, “Brain computer interfaces, a review,” *Sensors*, vol. 12, no. 2, pp. 1211–1279, 2012.
- [2] T. Milekovic, A. A. Sarma, D. Bacher, J. D. Simeral, J. Saab, C. Pandarinath, B. L. Sorice, C. Blabe, E. M. Oakley, K. R. Tringale, *et al.*, “Stable long-term bci-enabled communication in als and locked-in syndrome using lfp signals,” *Journal of Neurophysiology*, vol. 120, no. 7, pp. 343–360, 2018.
- [3] M. A. Van Gerven, B. Cseke, F. P. De Lange, and T. Heskes, “Efficient bayesian multivariate fmri analysis using a sparsifying spatio-temporal prior,” *NeuroImage*, 2010.
- [4] S. R. Damarla and M. A. Just, “Decoding the representation of numerical values from brain activation patterns,” *Human Brain Mapping*, 2013.
- [5] T. Horikawa and Y. Kamitani, “Generic decoding of seen and imagined objects using hierarchical visual features,” *Nature Communications*, 2017.
- [6] Y. Akamatsu, R. Harakawa, T. Ogawa, and M. Haseyama, “Brain decoding of viewed image categories via semi-supervised multi-view bayesian generative model,” *IEEE Transactions on Signal Processing*, 2020.
- [7] Y. Miyawaki, H. Uchida, O. Yamashita, M.-a. Sato, Y. Morito, H. C. Tanabe, N. Sadato, and Y. Kamitani, “Visual image reconstruction from human brain activity using a combination of multiscale local image decoders,” *Neuron*, vol. 60, no. 5, pp. 915–929, 2008.
- [8] S. Schoenmakers, M. Barth, T. Heskes, and M. Van Gerven, “Linear reconstruction of perceived images from human brain activity,” *NeuroImage*, vol. 83, pp. 951–961, 2013.
- [9] M. A. Van Gerven, F. P. De Lange, and T. Heskes, “Neural decoding with hierarchical generative models,” *Neural Computation*, vol. 22, no. 12, pp. 3127–3142, 2010.
- [10] R. Belyi, G. Gaziv, A. Hoogi, F. Strappini, T. Golan, and M. Irani, “From voxels to pixels and back: Self-supervision in natural-image reconstruction from fmri,” in *NeurIPS*, 2019.
- [11] G. Gaziv, R. Belyi, N. Granot, A. Hoogi, F. Strappini, T. Golan, and M. Irani, “Self-supervised natural image reconstruction and large-scale semantic classification from brain activity,” *NeuroImage*, 2022.
- [12] F. Ozcelik, B. Choksi, M. Mozafari, L. Reddy, and R. VanRullen, “Reconstruction of perceived images from fmri patterns and semantic brain exploration using instance-conditioned gans,” in *IJCNN*, 2022.
- [13] Z. Chen, J. Qing, T. Xiang, W. L. Yue, and J. H. Zhou, “Seeing beyond the brain: Conditional diffusion model with sparse masked modeling for vision decoding,” in *CVPR*, 2023.
- [14] Y. Takagi and S. Nishimoto, “High-resolution image reconstruction with latent diffusion models from human brain activity,” in *CVPR*, 2023.
- [15] L. Zhang and M. Agrawala, “Adding conditional control to text-to-image diffusion models,” *arXiv preprint arXiv:2302.05543*, 2023.
- [16] J. Sohl-Dickstein, E. Weiss, N. Maheswaranathan, and S. Ganguli, “Deep unsupervised learning using nonequilibrium thermodynamics,” in *ICML*, 2015.
- [17] J. Ho, A. Jain, and P. Abbeel, “Denoising diffusion probabilistic models,” in *NeurIPS*, 2020.
- [18] J. Song, C. Meng, and S. Ermon, “Denoising diffusion implicit models,” *arXiv:2010.02502*, 2020.
- [19] P. Dhariwal and A. Nichol, “Diffusion models beat gans on image synthesis,” in *NeurIPS*, 2021.

- [20] A. Vahdat, K. Kreis, and J. Kautz, “Score-based generative modeling in latent space,” in *NeurIPS*, 2021.
- [21] R. Rombach, A. Blattmann, D. Lorenz, P. Esser, and B. Ommer, “High-resolution image synthesis with latent diffusion models,” in *CVPR*, 2022.
- [22] W. Peebles and S. Xie, “Scalable diffusion models with transformers,” *arXiv:2212.09748*, 2022.
- [23] Z. Xiao, K. Kreis, and A. Vahdat, “Tackling the generative learning trilemma with denoising diffusion gans,” in *ICLR*, 2022.
- [24] A. Nichol, P. Dhariwal, A. Ramesh, P. Shyam, P. Mishkin, B. McGrew, I. Sutskever, and M. Chen, “Glide: Towards photorealistic image generation and editing with text-guided diffusion models,” *arXiv:2112.10741*, 2021.
- [25] Z. Kong, W. Ping, J. Huang, K. Zhao, and B. Catanzaro, “Diffwave: A versatile diffusion model for audio synthesis,” *arXiv:2009.09761*, 2020.
- [26] J. Liu, C. Li, Y. Ren, F. Chen, P. Liu, and Z. Zhao, “Diffsinger: Diffusion acoustic model for singing voice synthesis,” *arXiv:2105.02446*, 2021.
- [27] H. Li, Y. Yang, M. Chang, S. Chen, H. Feng, Z. Xu, Q. Li, and Y. Chen, “Srdiff: Single image super-resolution with diffusion probabilistic models,” *Neurocomputing*, 2022.
- [28] C. Saharia, J. Ho, W. Chan, T. Salimans, D. J. Fleet, and M. Norouzi, “Image super-resolution via iterative refinement,” *TPAMI*, 2022.
- [29] S. Gao, X. Liu, B. Zeng, S. Xu, Y. Li, X. Luo, J. Liu, X. Zhen, and B. Zhang, “Implicit diffusion models for continuous super-resolution,” *arXiv preprint arXiv:2303.16491*, 2023.
- [30] B. Poole, A. Jain, J. T. Barron, and B. Mildenhall, “Dreamfusion: Text-to-3d using 2d diffusion,” *arXiv:2209.14988*, 2022.
- [31] C.-H. Lin, J. Gao, L. Tang, T. Takikawa, X. Zeng, X. Huang, K. Kreis, S. Fidler, M.-Y. Liu, and T.-Y. Lin, “Magic3d: High-resolution text-to-3d content creation,” *arXiv:2211.10440*, 2022.
- [32] T. Anciukevičius, Z. Xu, M. Fisher, P. Henderson, H. Bilen, N. J. Mitra, and P. Guerrero, “Renderdiffusion: Image diffusion for 3d reconstruction, inpainting and generation,” *arXiv:2211.09869*, 2022.
- [33] M. Li, Y. Duan, J. Zhou, and J. Lu, “Diffusion-sdf: Text-to-shape via voxelized diffusion,” *arXiv:2212.03293*, 2022.
- [34] S. Luo and W. Hu, “Diffusion probabilistic models for 3d point cloud generation,” in *CVPR*, 2021.
- [35] J. Ho, T. Salimans, A. Gritsenko, W. Chan, M. Norouzi, and D. J. Fleet, “Video diffusion models,” in *NeurIPS*, 2022.
- [36] J. Ho, W. Chan, C. Saharia, J. Whang, R. Gao, A. Gritsenko, D. P. Kingma, B. Poole, M. Norouzi, D. J. Fleet, *et al.*, “Imagen video: High definition video generation with diffusion models,” *arXiv:2210.02303*, 2022.
- [37] D. Baranchuk, A. Voynov, I. Rubachev, V. Khrulkov, and A. Babenko, “Label-efficient semantic segmentation with diffusion models,” in *ICLR*, 2021.
- [38] G. Tevet, S. Raab, B. Gordon, Y. Shafir, D. Cohen-Or, and A. H. Bermano, “Human motion diffusion model,” *arXiv:2209.14916*, 2022.
- [39] B. Zeng, X. Liu, S. Gao, B. Liu, H. Li, J. Liu, and B. Zhang, “Face animation with an attribute-guided diffusion model,” *arXiv preprint arXiv:2304.03199*, 2023.
- [40] S. Chen, P. Sun, Y. Song, and P. Luo, “Diffusion-det: Diffusion model for object detection,” *arXiv:2211.09788*, 2022.
- [41] V. Kulikov, S. Yadin, M. Kleiner, and T. Michaeli, “Sinddm: A single image denoising diffusion model,” *arXiv:2211.16582*, 2022.
- [42] W. Wang, J. Bao, W. Zhou, D. Chen, D. Chen, L. Yuan, and H. Li, “Sindiffusion: Learning a diffusion model from a single natural image,” *arXiv:2211.12445*, 2022.
- [43] T. Naselaris, R. J. Prenger, K. N. Kay, M. Oliver, and J. L. Gallant, “Bayesian reconstruction of natural images from human brain activity,” *Neuron*, vol. 63, no. 6, pp. 902–915, 2009.
- [44] K. N. Kay, T. Naselaris, R. J. Prenger, and J. L. Gallant, “Identifying natural images from human brain activity,” *Nature*, 2008.
- [45] S. Nishimoto, A. T. Vu, T. Naselaris, Y. Benjamini, B. Yu, and J. L. Gallant, “Reconstructing visual experiences from brain activity evoked by natural movies,” *Current biology*, vol. 21, no. 19, pp. 1641–1646, 2011.
- [46] N. Kriegeskorte, E. Formisano, B. Sorger, and R. Goebel, “Individual faces elicit distinct response patterns in human anterior temporal cortex,” *Proceedings of the National Academy of Sciences*, vol. 104, no. 51, pp. 20600–20605, 2007.

- [47] D. L. Yamins, H. Hong, C. F. Cadieu, E. A. Solomon, D. Seibert, and J. J. DiCarlo, “Performance-optimized hierarchical models predict neural responses in higher visual cortex,” *Proceedings of the National Academy of Sciences*, vol. 111, no. 23, pp. 8619–8624, 2014.
- [48] D. C. Van Essen, S. M. Smith, D. M. Barch, T. E. Behrens, E. Yacoub, K. Ugurbil, W.-M. H. Consortium, *et al.*, “The wu-minn human connectome project: an overview,” *NeuroImage*, 2013.
- [49] A. Radford, J. W. Kim, C. Hallacy, A. Ramesh, G. Goh, S. Agarwal, G. Sastry, A. Askell, P. Mishkin, J. Clark, *et al.*, “Learning transferable visual models from natural language supervision,” in *ICML*, 2021.
- [50] J. Deng, W. Dong, R. Socher, L.-J. Li, K. Li, and L. Fei-Fei, “Imagenet: A large-scale hierarchical image database,” in *CVPR*, 2009.
- [51] N. Chang, J. A. Pyles, A. Marcus, A. Gupta, M. J. Tarr, and E. M. Aminoff, “Bold5000, a public fmri dataset while viewing 5000 visual images,” *Scientific data*, 2019.
- [52] J. Xiao, J. Hays, K. A. Ehinger, A. Oliva, and A. Torralba, “Sun database: Large-scale scene recognition from abbey to zoo,” in *CVPR*, 2010.
- [53] T.-Y. Lin, M. Maire, S. Belongie, J. Hays, P. Perona, D. Ramanan, P. Dollár, and C. L. Zitnick, “Microsoft coco: Common objects in context,” in *ECCV*, 2014.
- [54] I. Loshchilov and F. Hutter, “Decoupled weight decay regularization,” in *ICLR*, 2017.
- [55] D. P. Kingma and J. Ba, “Adam: A method for stochastic optimization,” in *ICLR*, 2015.
- [56] A. Dosovitskiy, L. Beyer, A. Kolesnikov, D. Weissenborn, X. Zhai, T. Unterthiner, M. Dehghani, M. Minderer, G. Heigold, S. Gelly, *et al.*, “An image is worth 16x16 words: Transformers for image recognition at scale,” *arXiv preprint arXiv:2010.11929*, 2020.
- [57] Z. Wang, A. C. Bovik, H. R. Sheikh, and E. P. Simoncelli, “Image quality assessment: from error visibility to structural similarity,” *TIP*, 2004.